Contribution of gravity waves to universal vertical wavenumber (m^{-3}) spectra revealed by a gravity-wave-permitting general circulation model

Haruka Okui[1], Kaoru Sato[1], and Shingo Watanabe[2]

[1]Department of Earth and Planetary Science, Graduate School of Science, The University of Tokyo, Tokyo, Japan

[2]Japan Agency for Marine–Earth Science and Technology, Yokohama, Japan

Corresponding author: Haruka Okui (`okui@eps.s.u-tokyo.ac.jp`)

Key Points:

- Using a gravity-wave-permitting high-top general circulation model, gravity wave spectra in the middle atmosphere were examined.

- Characteristics of the model-simulated vertical wavenumber (m) spectra of gravity waves are broadly consistent with observations.

- Disturbances other than gravity waves contribute substantially to the lowest m part of the m^{-3} range.

Index Terms

3255 Spectral analysis, 3332 Mesospheric dynamics, 3334 Middle atmosphere dynamics, 3363 Stratospheric dynamics, 3384 Acoustic-gravity waves

Key Words

Gravity waves, middle atmosphere, spectral analysis

Abstract

Observations with high vertical resolution have revealed that power spectra of horizontal wind and temperature fluctuations versus the vertical wavenumber m have common shape with a steep slope of ~m^{-3}. Several theoretical models explaining this spectral slope were proposed on the basis of an assumption of gravity wave (GW) saturation. However, there is little to confirm that such observed spectra are fully composed of GWs. To examine whether the m^{-3} spectra are attributable to GWs, spectral analysis of GWs in the middle atmosphere was conducted using a GW-permitting high-top general circulation model. The

model-simulated spectra have steep spectral slopes consistent with observations. GWs were extracted as fluctuations having total horizontal wavenumbers of 21–639. Comparison of the spectra of GWs with those of all simulated fluctuations revealed that GWs dominate only when m is high, whereas disturbances other than GWs largely contribute to the spectra when m is low, even in the m^{-3} range. Additionally, vertical and geographical distributions of the characteristic wavenumbers, slopes, and amplitudes of GW spectra were also examined. It is inferred that strong vertical shear below the eastward and westward jets is responsible for the formation of the steep spectral slopes of GWs.

Plain Language Summary

Radar and radiosonde observations have revealed that vertical wavenumber power spectra of horizontal wind and temperature fluctuations have common shape with a steep slope. Several theoretical studies have explained this universality by assuming that these spectra are composed of saturated gravity waves (GWs). To examine whether such universal spectra are attributable to GWs, spectral analysis of GWs, having short horizontal wavelengths, was conducted using a GW-permitting high-top general circulation model. The model-simulated spectra have steep spectral slopes consistent with observations. Comparison of the spectra of GWs with those of all simulated fluctuations revealed that disturbances other than GWs also contribute to the spectra at a lowest-wavenumber part of a steep slope. Additionally, vertical and geographical variations of characteristics of GW spectra were described. It is inferred that strong vertical shear below the eastward and westward jets is responsible for steepening GW spectral slopes. As well as deepening our understanding of GWs in the middle atmosphere, these findings provide guidelines for improving representation of GWs in climate models using GW parameterizations.

1 Introduction

Gravity waves (GWs) are small-scale atmospheric waves that play fundamental roles in determining the large-scale dynamic and thermal structure of the middle atmosphere by transporting momentum and energy (e.g., Fritts and Alexander, 2003). For example, GW forcing contributes substantially to both maintaining the weak wind layer near the mesopause and driving the meridional circulation in the mesosphere. Equatorial stratospheric and mesospheric quasi biennial oscillations (QBOs) are mainly driven by GWs originating from the troposphere (e.g., Sato & Dunkerton, 1997; Kawatani et al., 2010a, 2010b; Mayr et al., 1997). It has also been shown that GWs cause extension of the deep branches of the Brewer–Dobson circulation to higher latitudes, and determination of the location of the turnaround latitude of the circulation (e.g., Okamoto et al., 2011; Sato & Hirano, 2019).

On the basis of radar and radiosonde observations, it has been established that

power spectra versus the vertical wavenumber (m) of horizontal wind and temperature fluctuations have common shape with a steep slope (e.g., VanZandt, 1982, 1985; Dewan et al., 1984; Dewan & Good, 1986; Fritts & Chou, 1987; Tsuda et al., 1989, 1990; Allen & Vincent, 1995; Sato et al., 2003). These 'universal' spectra are approximately, but not necessarily, proportional to m^{-3} in a m range higher than the characteristic wavenumber m_*. Several theories have been developed regarding these characteristic m spectra. Adopting a concept of superposition of saturated GWs, Smith et al. (1987) developed a theoretical model that explains that the horizontal wind spectrum varies as $N^2/6m^3$ for $m \gtrsim m_*$, where N is the buoyancy (Brunt–Väisälä) frequency. They assumed that the spectral range occupied by a single saturated GW (Δm) is proportional to m (Dewan & Good, 1986). Sato and Yamada (1994) examined the change in m in the linear vertical shear of the background wind parallel to the horizontal wavenumber vector and derived a theoretical spectrum of a single saturated GW without the assumption of $\Delta m \propto m$. The spectral form of the horizontal wind fluctuations shown by Sato and Yamada (1994) can be expressed as follows:

$$P_u(m) \approx N^3 \cdot \left(2m^4 \cdot \Delta z \left| \mathrm{d}U/\mathrm{d}z \right| \right)^{-1} \sqrt{N^2/m^2 + f^2/k^2}, \quad (1)$$

where Δz is the height expanse for the spectrum calculation, k is the horizontal wavenumber, and f is the Coriolis parameter. These theoretical models succeeded in explaining the characteristic shape and level of the m spectra. However, it has not been fully confirmed that the observed m spectra are totally attributable to GWs. A recently available GW-permitting general circulation model (GCM) represents an interesting and useful research tool suitable for providing this confirmation, because GWs can be extracted as fluctuations having high total horizontal wavenumbers. Theories describing m spectra form the basis of nonorographic GW parameterizations (e.g., Lindzen, 1981; Hines, 1997a, 1997b; Warner & McIntyre, 1996, 1999; Alexander & Dunkerton, 1999) used widely in climate models. Descriptions of vertical and horizontal variations of GW spectra in a GW-permitting model can provide useful guidelines for improving representation of GWs in models using GW parameterizations (e.g., McLandress & Scinocca, 2005; Watanabe, 2008).

In this study, we used outputs from a hindcast of December 2018 using a GW-permitting GCM extending from the surface to the lower thermosphere (Okui et al., 2021). The GWs were extracted as fluctuations having total horizontal wavenumbers of 21–639. First, it was verified that the model could reproduce the main observed spectral properties. Next, to examine the contribution of GWs to the spectra in the m^{-3} range, m spectra of GWs and all fluctuation components obtained from each single profile, just as they were extracted from radar or radiosonde observations, were compared. Global distributions of parameters describing the characteristics of GW spectra were also examined for each height region in the middle atmosphere. The remainder of this paper is structured as

3

follows. Detailed descriptions of the model and the analysis method are given in Section 2. Results are discussed in Section 3. A summary and concluding remarks are presented in Section 4.

2 Method and Model Description

The model used in this study is a high-resolution version of the Japanese Atmospheric GCM for Upper Atmosphere Research (JAGUAR) (Watanabe & Miyahara, 2009). This model comprises 340 vertical layers from the surface to the geopotential height of ~150 km, with a log-pressure height interval of 300 m throughout the middle atmosphere, and it has a horizontal-triangularly truncated spectral resolution of T639, whose minimum resolvable horizontal wavelength is ~60 km. No parameterizations for subgrid-scale GWs were used in the present study.

A hindcast was performed for 5 December 2018 to 17 January 2019 using global analysis data produced by the JAGUAR–Data Assimilation System (JAGUAR-DAS) (Koshin et al., 2020, 2021) in a medium-resolution (T42L124) version of the JAGUAR as initial data. A four-dimensional local ensemble transform Kalman filter and a filter called incremental analysis updates (Bloom et al., 1996) are used in the JAGUAR-DAS. The PrepBUFR observational dataset provided by the National Centers for Environmental Prediction, satellite temperature data from the Aura Microwave Limb Sounder and the Sounding of the Atmosphere using Broadband Emission Radiometry on the Thermosphere, Ionosphere, Mesosphere Energetics Dynamics satellite, and brightness temperature data from the Special Sensor Microwave Imager/Sounder were assimilated. The hindcast period was divided into consecutive 4-day intervals, for each of which an independent run was performed using the high-resolution JAGUAR. Each model run consisted of a spectral nudging run over 3 days and a free run over the subsequent 4 days. We analyzed the outputs at 1-hour intervals from the 4-day free runs only for the 5–20 December 2018. We did not use data from later periods because substantial modulation of GW fields was expected in association with the onset of major sudden stratospheric warming on 1 January 2019. Detailed analysis of this sudden stratospheric warming is presented in Okui et al. (2021).

In the present study, GWs were defined as fluctuations having total horizontal total wavenumbers of 21–639 (horizontal wavelengths of $\lambda_h <$ 2000 km). To imitate the extraction methods of fluctuations in radar and radiosonde observations and to compare the results with GW spectra, unfiltered individual vertical profiles of zonal wind, meridional wind, and temperature with their linear trends removed were also used in the spectral calculations. Temperature fluctuations were multiplied by $g/T_0 N$, where T_0 is the background temperature extracted as a linear trend from each unfiltered temperature profile, and g is gravitational acceleration. Because the obtained power spectra had steep slopes, i.e., proportional to $\sim m^{-3}$, prewhitening and recoloring processes were performed before

4

and after the calculation of spectra, respectively (e.g., Sato et al. 2003). The degree of prewhitening β was taken as 0.95 in this study. Profiles having finite data length were tapered using a 10% cosine-tapered window for the first and last tenth of the data series. Using a Fast Fourier Transform, power spectra were calculated from these processed profiles of GWs having $n = 21$–639 and unfiltered fluctuation components; hereafter, referred to as all fluctuations. For accurate estimation of the amplitudes of the spectra under the effect of the window function, the calculated spectra were multiplied by a factor $1/0.875$.

3 Results and Discussion

3.1 Contribution of GWs to m^{-3} spectra

The zonal wind, meridional wind, and temperature spectra from 5–20 December 2018 at Shigaraki (35°N, 136°E), Japan, where the MU radar is located, are shown in Figs. 1a–c, respectively, for the lower stratosphere and in Figs. 1d–f, respectively, for the middle and upper mesosphere. The height regions for the spectra were determined such that N^2 is approximately constant, as assumed in Smith et al. (1987).

It is important that the model-simulated spectra of all fluctuations have a shape with a steep slope of $\sim m^{-3}$ in the high m range in both the lower stratosphere and the mesosphere. This feature is consistent with the spectra calculated from MU radar observations (e.g., Tsuda et al., 1989). The m^{-3} range of the spectra is in good agreement with the theoretical spectral model derived by Smith et al. (1987). The GW spectra are bent at a specific value of m of 3–5×10^{-4} m^{-1} in the lower stratosphere and 1–2×10^{-4} m^{-1} in the mesosphere. In the m range above the bending point, the GW spectra are nearly proportional to m^{-3} and they agree well with those of all fluctuations. At lower values of m, the spectral density of the GW spectra is smaller than that of all fluctuations, even within the m^{-3} range of the all fluctuation spectra. These facts suggest that the observed spectral slopes of $\sim m^{-3}$ mainly consist of GWs in the high m range, but that disturbances other than GWs also contribute substantially to the spectra at lower values of m within the m^{-3} range. The highest m in the range where there is disagreement between the spectra of GWs and those of all fluctuations is lower in the mesosphere than in the lower stratosphere. This difference shows that GWs are dominant in a lower m range in the mesosphere.
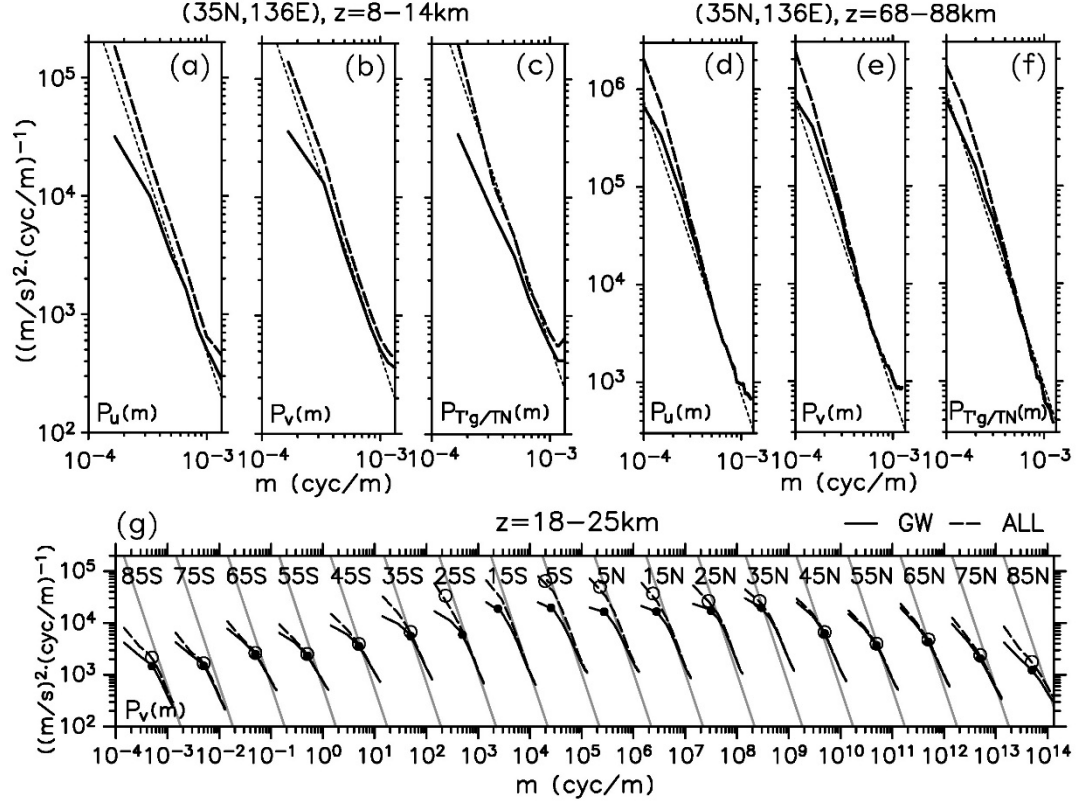
A series of meridional wind spectra in the middle stratosphere for $z = 18$–25 km, averaged over the latitudinal range of $\pm 5°$ around each latitude, are shown in Fig. 1g. To estimate the parameters describing the characteristics of these spectra, the obtained spectral curves were fitted to the following equation (Allen & Vincent, 1995) using a trust-region algorithm (Conn et al., 2000):

$$P_{\mathrm{ALL}}(m) = F_0 \frac{m/m_*}{1+(m/m_*)^{t+1}}, \quad P_{\mathrm{GW}}(m) = F_0 \frac{m/m_{g*}}{1+(m/m_{g*})^{t+1}}, \quad (2a, 2b)$$

where m_* in Eq. (2a) and m_{g*} in Eq. (2b) are the characteristic wavenumbers (approximate bending wavenumbers) of an all fluctuation spectrum $P_{\mathrm{ALL}}(m)$ and the GW spectrum $P_{\mathrm{GW}}(m)$, respectively; F_0 is a parameter representing the amplitude at $m = m_*$ or m_{g*}; and t represents the spectral slope of opposite sign. The closed (open) circles in Fig. 1g represent m_{g*} (m_*) estimated for each spectrum.

The spectra at latitudes of 45°S–35°N have shape with an ~m^{-3} slope at higher values of m. However, the spectral slopes at higher latitudes are relatively gentle and almost proportional to ~m^{-2}, even in the high range of m values. Similar to the case of Shigaraki (Figs. 1a–f), the difference in spectral density between the GWs and all fluctuations is substantial at $m < m_{g*}$ except at 45°–75°S, where GWs appear dominant, even at low values of m. The difference is particularly large at low latitudes of 25°S–25°N and in the polar regions at 85°S and 85°N. The folding wavenumber for the all fluctuation spectra is slightly (~1.1–2 times) smaller than m_{g*} at 25°S–25°N.

It is considered that the contribution of equatorial waves to the spectral densities is large at low latitudes near the equator. Because meridional wind fluctuations are examined here, Rossby-gravity waves, not Kelvin waves, are possible candidates for such waves. However, the approximate meridional scale of equatorial waves is ~1500 km (~7°S–7°N). Therefore, these waves cannot account for the additional spectral density at 25°S and 25°N. Inertial instability is another possible reason for the meridional wind structure having a vertical wavelength of ~1–2 × 10^{-4} m^{-1} (e.g., Dunkerton, 1981). However, anomalous potential vorticity, which is the inertially unstable condition, is rarely observed at $z = 18$–25 km (not shown). Secondary circulation associated with the QBO has a larger vertical scale than the range of m^{-1} discussed here. The cause of the differences between GW and all fluctuation spectra at low latitudes is left for future studies. As for the spectra at 85°S and 85°N, the difficulty in handling zonal and meridional wind fluctuations near the poles, combined with total horizontal wavenumber filtering, might have affected the results.

Figure

1 Vertical wavenumber spectra from 5–20 December 2018 of (a, d) zonal wind, (b, e) meridional wind, and (c, f) temperature fluctuations at Shigaraki (35°N, 136°E), Japan, in the height regions of (a–c) $z = 8$–14 and (d–f) 68–88 km. Solid and dashed curves show the spectra of GWs and all fluctuation components, respectively. Theoretical spectra from Smith et al. (1987) are indicated by thin dotted lines. (g) Meridional wind spectra from 5–20 December 2018 at z =18–25 km averaged zonally and over the respective latitude regions of ±5° of the center of the latitudes shown in the figure. Closed (open) circles indicate the folding point of GW (all fluctuation) spectra. Gray lines are the theoretical spectra from Smith et al. (1987). The scale of the horizontal axis is for the spectra at 85°S and curves for the other latitudes are shifted by an order of magnitude one by one.

3.2 Characteristics of GW spectra in the middle atmosphere

To examine the behavior of GWs in the middle atmosphere, the vertical and geographical distributions of parameters m_{g*}, F_0, and t in Eq. (2b) were estimated. Figure 2 shows the zonally averaged parameters at each height region as functions of latitude. The height regions used for calculation were deter-

7

mined such that N^2 was almost constant in each region. The main features of the parameter distributions for the zonal wind spectra (Figs. 2a–c), meridional wind spectra (Figs. 2d–f), and temperature spectra (Figs. 2g–i) are generally consistent. The following discussion is based on the parameters of meridional wind spectra, but similar results were obtained for both the zonal wind and the temperature spectra.

It can be seen that the value of m_{g*} is lower at higher altitudes (Fig. 2a). This is consistent with the theoretical expectation of Smith et al. (1987). The values of m_{g*} in the middle and upper mesosphere at $z = 60$–90 km are 1/3–2/3 of those in the lower stratosphere at $z = 18$–33 km. Parameter F_0 is larger in higher altitude regions (Fig. 2c). The values of F_0 at $z = 60$–90 km are 50–200 times larger than those at $z = 18$–33 km. Adopting the concepts of wave amplification with height and GW saturation, it is theoretically estimated that the ratio of m_{g*} at $z = 60$–90 km to that at $z = 18$–33 km is ~1/6–1/3, and that the ratio of F_0 at $z = 60$–90 km to that at $z = 18$–33 km is ~40–240 (Smith et al., 1987). The model results broadly agree with these theoretical estimates. Thus, the vertical variations of the parameters are mostly explained by amplification of saturated GWs due to the exponential decrease in atmospheric density. However, vertical variation in m_{g*} is slightly more moderate than that of the theoretical estimates. One possible explanation for the departure from theory is that the assumption of GW saturation is not necessarily fulfilled. While t is approximately constant at 15°S–25°N, t is 1.5–1.8 at $z = 18$–33 km and it approaches ~3 with height at mid- and high latitudes. The possible cause of both the moderate vertical variation in m_{g*} and the variation in t is discussed in Section 3.3.

In terms of latitudinal variation, m_{g*} has a maximum value of 2.2–2.5 $\times$ 10^{-4} m^{-1} at 20°S–40°N in the lower and middle stratosphere (i.e., $z = 18$–33 km and $z = 33$–45 km, respectively). It is almost homogeneous in the uppermost stratosphere and mesosphere ($z = 45$–60 km and $z = 60$–90 km, respectively). In the uppermost stratosphere and lowermost mesosphere at $z = 45$–60 km, t has two significant peaks of ~2.7 at ~15°S and ~3 at ~50°N. As for the F_0 distribution, there are two peaks of ~3 $\times$ 10^4 m^3 s^{-2} at ~15°S and ~4 $\times$ 10^4 m^3 s^{-2} at 50°–75°N in the lower stratosphere ($z = 18$–33 km). The peak in the Northern Hemisphere is broader in higher altitude regions. The peak at ~15°S shifts to higher latitudes at higher altitudes, consistent with the poleward propagation of eastward GWs due to refraction toward the summer westward jet (e.g., Sato et al., 2009).

Figure 3 illustrates longitude–latitude maps of m_{g*}, t, and F_0 at $z = 18$–33 km in the lower stratosphere. The contours represent zonal wind. In the high latitudes of the Northern Hemisphere, m_{g*} is small along the eastward jet. It is considered that a major part of GWs generated in the troposphere must pass through the weak wind layer at around 20 km upward. Thus, most GWs that do not encounter their critical levels should have small ground-based phase velocities c in the eastward jet in the middle atmosphere. Therefore, small m_{g*} near the eastward jet is consistent with the theoretical expectation that the m

of a GW having small c becomes small when U is strong, i.e., $m^2 \approx N^2/(c-U)^2$. In the low-latitude region, especially 20°S–10°N, both m_{g*} and t are large. In contrast to the effect of the jet at high latitudes, these large m_{g*} and t values are likely attributable to a zero-wind line at 15°S–15°N (not shown) associated with the QBO, which results in smaller $(c - U)$ and larger m, making wave saturation more likely. The geographical distribution of m_{g*} is consistent (i.e., has negative correlation) with that of the vertical wavelengths of GWs having large amplitude in boreal winter (but in January, not December) derived from satellite observations by Ern et al. (2018). It is notable that F_0 has peaks along the eastward jet in the Northern Hemisphere, at low latitudes in the Southern Hemisphere, and around South America. This geographical distribution of the peaks of F_0 is broadly consistent with that of the peaks of GW amplitudes derived from satellite observations by Ern et al. (2018). Sato et al. (2009) suggested that steep mountains, the upper-tropospheric eastward jet in winter, and subtropical monsoon convection in summer act as dominant GW sources. These GW sources might contribute to the observed F_0 peaks.

Maps of the parameter in the uppermost stratosphere and lowermost mesosphere at $z = 45$–60 km are shown in Fig. 4. Interestingly, t in the eastward jet region in the Northern Hemisphere is notably high, ranging from 3–3.75. At low latitudes in the Southern Hemisphere, t is also relatively high along the westward jet. As mentioned above, the m of a GW becomes small where U is strong because of the small intrinsic phase velocity. Because $N^2/m^2 \gg f^2/k^2$ in Eq. (1), which was derived by Sato and Yamada (1994) for a GW propagating in linear wind shear, the spectral slope approaches -4. The distributions of m_{g*} and F_0 in the lower mesosphere (Figs. 4a and 4c, respectively) have less spatial variability than those in the lower stratosphere (Figs. 3a and 3c, respectively). This spatial uniformity was also observed in the middle and upper mesosphere at $z = 60$–90 km (not shown).
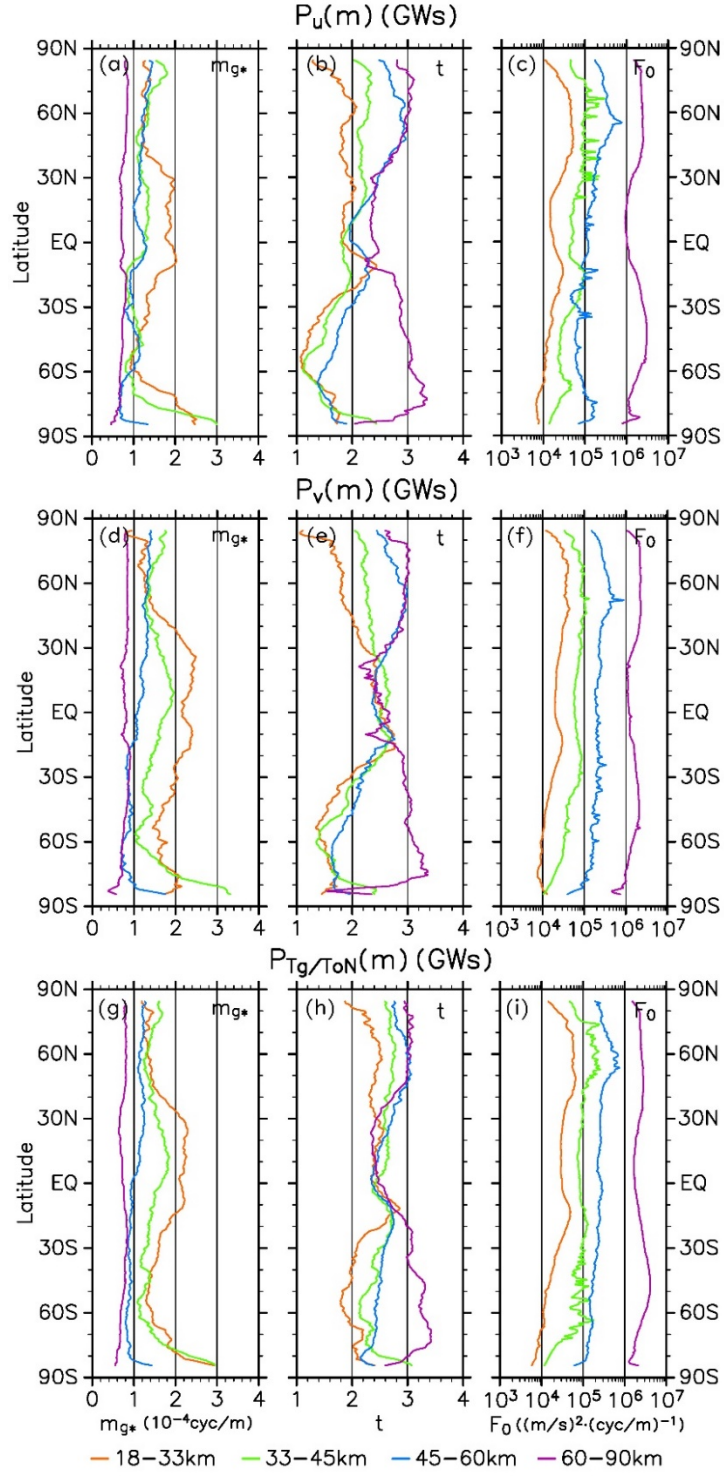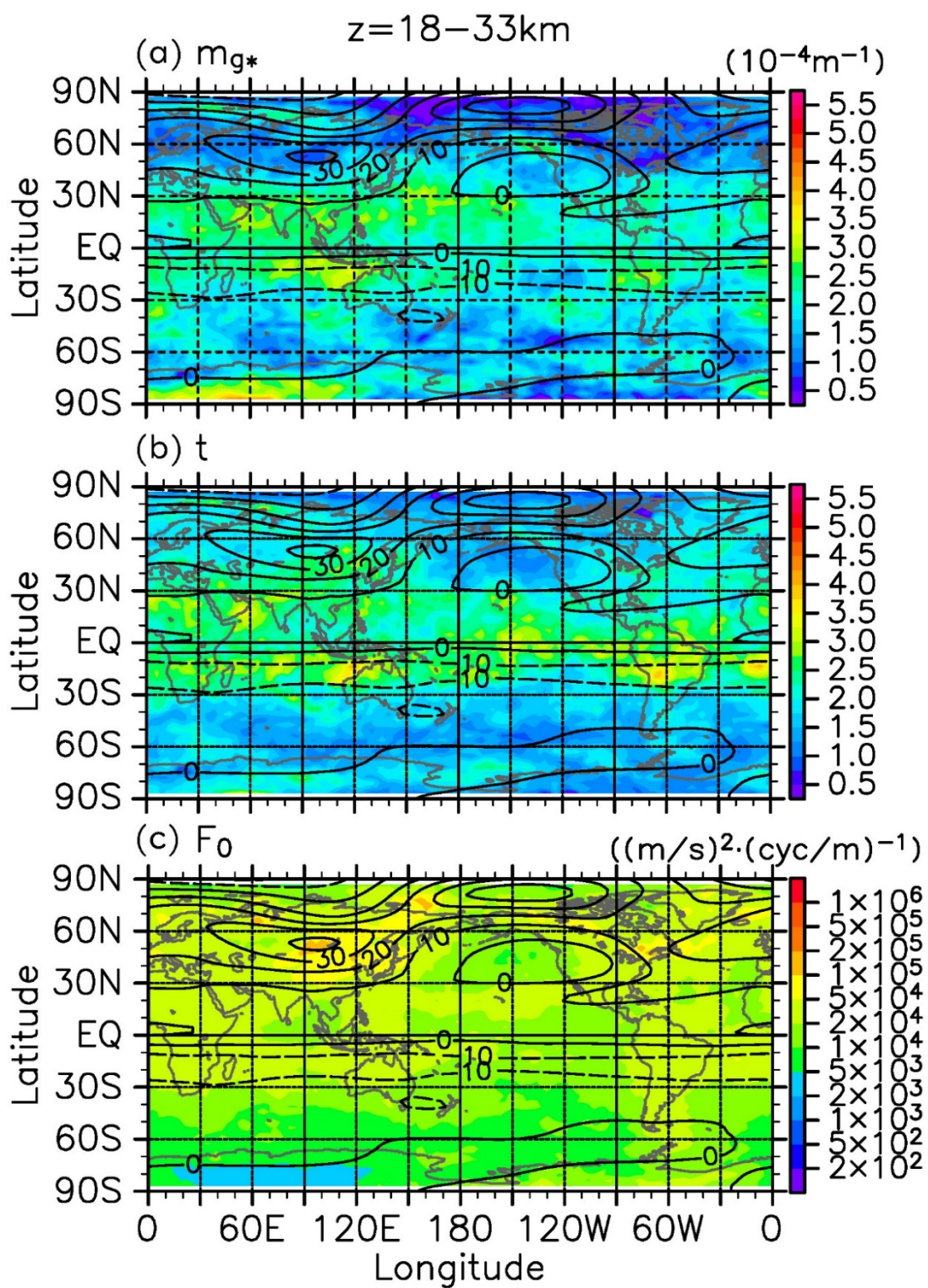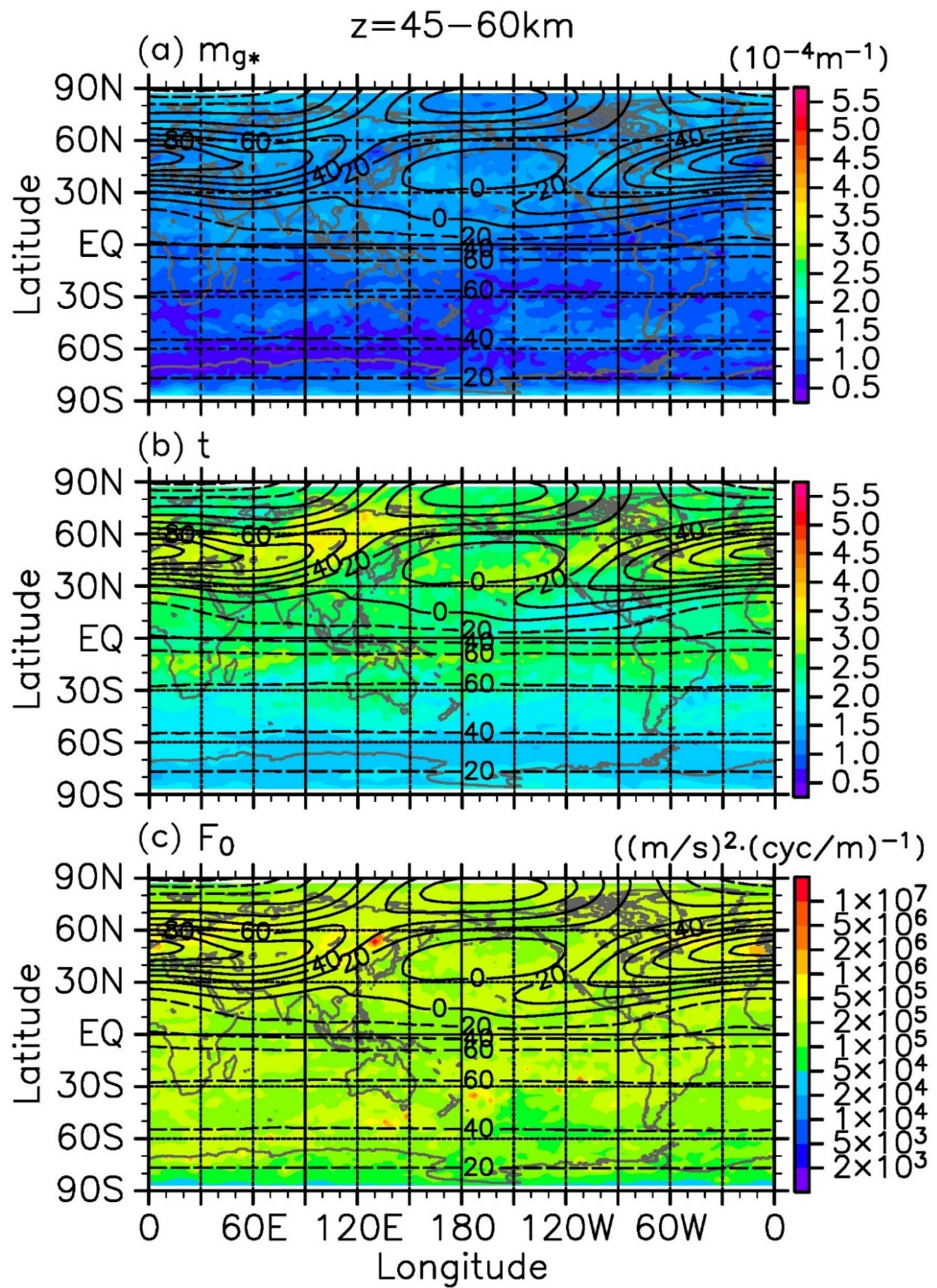
Figure 2 Zonal

mean m_{g*}, t, and F_0 of (a–c) zonal wind, (d–f) meridional wind, and (g–i) temperature spectra of GWs from 5–20 December 2018 as functions of latitude. The color of the curves represents the height region: $z = 18$–33 km (orange), 33–45 km (green), 45–60 km (blue), and 60–90 km (purple).

z=18−33km

(a) m_{g*}

$(10^{-4}m^{-1})$

(b) t

(c) F_0

$((m/s)^2 \cdot (cyc/m)^{-1})$

Longitude

Figure

3 Maps of (a) m_{g*}, (b) t, and (c) F_0 for meridional wind spectra of GWs in the lower stratosphere at $z = 18$–30 km from 5–20 December 2018. Contours show zonal wind.

z=45−60km

(a) m_{g*} $(10^{-4}m^{-1})$

(b) t

(c) F_0 $((m/s)^2 \cdot (cyc/m)^{-1})$

14

Figure

4 Similar to Fig. 3 but for the uppermost stratosphere and lowermost mesosphere at $z = 45$–60 km from 5–20 December 2018. Note that the colormap used in Fig. 4c and the contour interval are different from those used in Fig. 3d.

3.3 Shear effect on vertical variation of GW spectra

At mid- and high latitudes below the height of $z = 45$–60 km, the spectral slope becomes steeper with height (Figs. 2b and 2e). Additionally, the decrease in m_{g*} with height, which is expected when GWs are saturated, is much smaller than that at low latitudes (Figs. 2a and 2d). Such a characteristic vertical change in the m spectra is particularly clear around the latitudes of the mesospheric eastward and westward jets (Fig. 4). Here, the effect of strong vertical shear below the jets on the shape of a GW spectrum is examined.

Consider a GW propagating in a background wind $U(z)$ that is parallel to the m vector and varies only in the vertical. The dispersion relation for a hydrostatic and nonrotational internal GW is as follows:

$$\hat{\omega} = \frac{n^2 N^2}{m^2}, \quad (3)$$

where $\hat{\omega}$ is the intrinsic frequency. We can take the sign of $\hat{\omega}$ as positive without loss of generality. Under this setting, the vertical m is negative for a GW having an upward group velocity. Thus, based on the Wentzel–Kramers–Brillouin approximation, the variation of $m = m(U; z)$ is as follows:

$$m(U; z) = -\frac{N}{|c - U(z)|}. \quad (4)$$

This equation yields the z derivative of $m(U; z)$:

$$\frac{dm}{dz} \left(= -\frac{d|m|}{dz} \right) = \frac{dm}{dU} \frac{dU}{dz} = \frac{m^2}{N} \frac{U - c}{|U - c|} \frac{dU}{dz}. \quad (5)$$
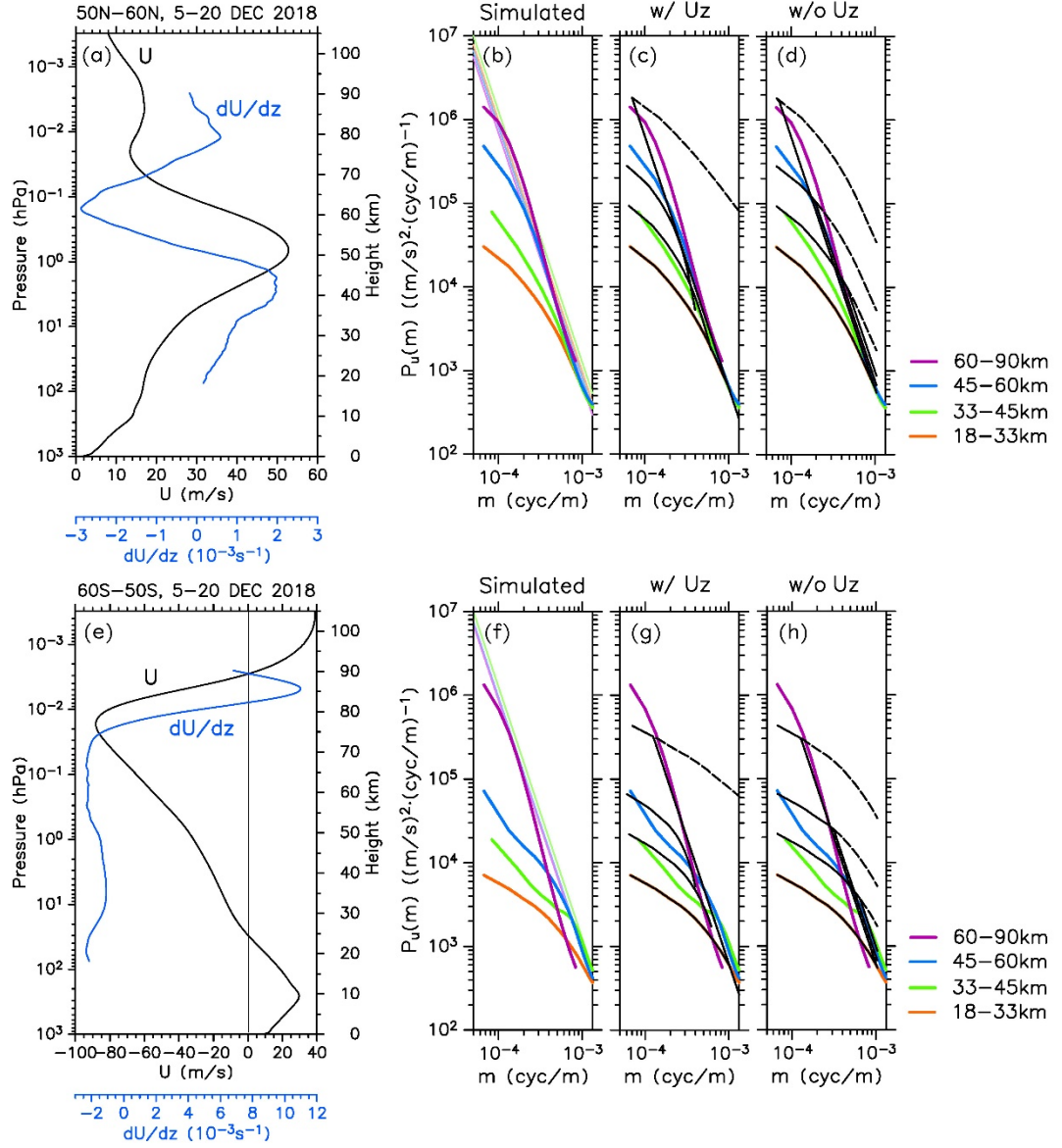
Here, we assume that dominant GWs have reasonably small ground-based phase velocity, i.e., $c = \sim 0$, as before. For such GW, both $U - c$ and dU/dz are positive (negative) below the eastward (westward) jet. Thus, the rightmost side of the Eq. (5) is positive and larger for higher $|m|$ (note that it is proportional to m^2). This fact indicates that the absolute wavenumber $|m|$ decreases more quickly with height in a higher $|m|$ range. It is considered that this vertical shear effect on a GW spectrum results in the increase in t below the peak of a jet.

To evaluate this shear effect quantitatively, the z derivative of $|m|$ in Eq. (5) was integrated numerically for the zonal wind spectra of GWs at 50°–60°N around

the eastward jet and at 50°–60°S around the westward jet. The calculation was performed using model-simulated spectra for $z = 18$–33 km as initial values. The initial height for the integration was chosen as $z = 25.5$ km, i.e., the center of the range of 18–33 km. The vertical variation in spectral density was estimated using Eq. (16) of Smith et al. (1987), i.e., $P(m) \propto e^{z/(2H_E/3)}$, where H_E is in the range of 14–21 km. Here, we took 18 km for the value of H_E. Profiles of the background zonal wind U averaged zonally and over the respective latitude regions are shown in Figs. 5a and 5e, respectively. The spectra obtained by the above calculation are shown by black curves in Figs. 5c and 5g, which are overlayed on the model-simulated spectra shown by colored curves (same as in Figs. 5b and 5f). Note that m for the horizontal axes of these figures means $|m|$. Each black curve shows the result at the center of each height region (i.e., $z = 39.0$, 52.5, and 75.0 km). The results of the calculation without the shear effect on m are shown in Figs. 5d and 5h for comparison. When a calculated spectrum exceeds the spectral density of the theoretical spectrum of Smith et al. (1987) (i.e., $N^2/12m^3$), shown by the light-colored curves in Figs. 5b and 5f, we consider that the spectral density is limited to that of the theoretical spectrum attributable to wave saturation. The spectra without this limitation of wave saturation are shown by the dashed curves.

For both latitude regions, the estimated spectra with shear effect (Figs. 5c and 5g) accord better with the model-simulated spectra than the spectra estimated without the shear effect (Figs. 5d and 5h), especially for $z = 33$–45 km at 50°–60°N, and $z = 33$–45 and 45–60 km at 60°–50°S. However, there are a few exceptions. In the uppermost stratosphere and lowermost mesosphere ($z = 45$–60 km) at 50°–60°N, the estimated spectral density with shear effect is smaller than the model-simulated spectrum (denoted by the blue curve). In this region, the kinetic energy of GWs increases rapidly with height, as shown in Fig. 6. Thus, GWs having large amplitude near the top of the height region (i.e., $z = 60$ km) contribute substantially to the model-simulated spectrum. Such inhomogeneity of the variance in the vertical within the range for which the spectra are calculated might explain the difference between the model-simulated spectrum and the estimated spectrum.
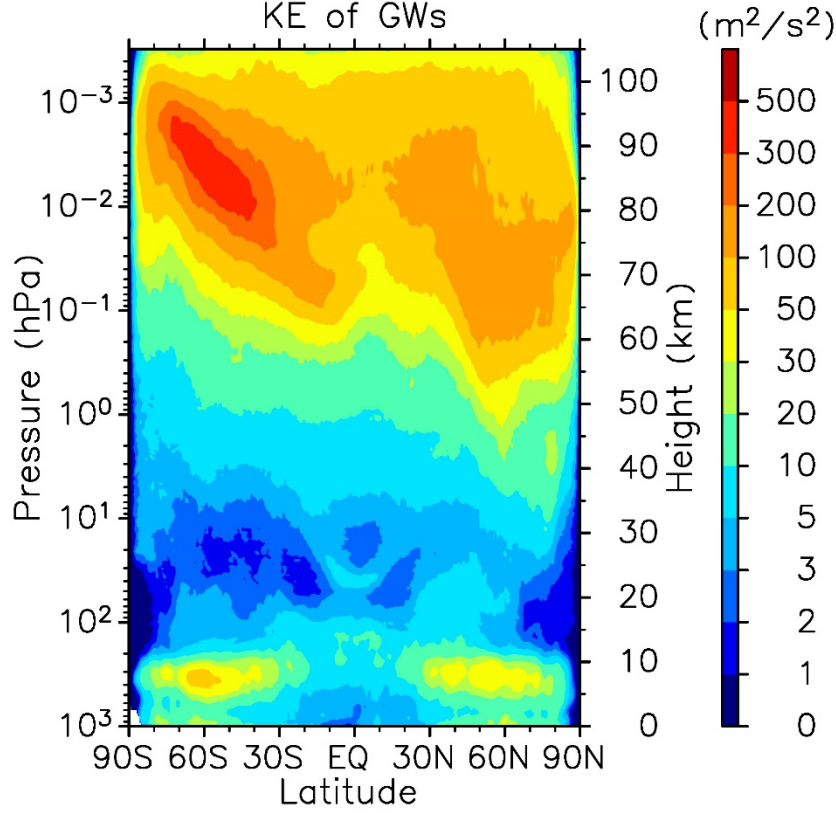
Even in the m range where the wave-saturation threshold is not fulfilled (i.e., without dashed curves), these estimates of shear-affected spectra show the increase in spectral slope that is also seen in the model-simulated spectra. The most interesting suggestion here is that the steep slope of a GW m spectrum is likely formed by strong vertical shear, even in the absence of wave saturation.

Figure

5 Estimates of the shear effect on GW spectra at (a–d) 50°–60°N and (e–h) 60°–50°S from 5–20 December 2018. (a, e) Vertical profiles of background zonal winds U averaged zonally and over the shown latitude regions. Blue curves represent dU/dz, which was used for the calculation. (b, f) Model-simulated spectra (colored curves; legends are shown on the right). Curves with the same but lighter colors show theoretical spectra (Smith et al., 1987), which almost overlap with each other. (c, g) Estimated spectra with shear effect (black curves). (d, h) Estimated spectra without shear effect (black curves). These

17

spectra are overlayed on the model-simulated spectra in the respective height regions. Dashed curves represent the results with wave saturation ignored.

Figure 6 Latitude–height section of zonal mean kinetic energy of GWs from 5–20 December 2018.

4 Summary and Concluding Remarks

Using the output of a hindcast of December 2018 performed by a GW–permitting high-top GCM, we examined the contribution of GWs to the universal vertical wavenumber (m^{-3}) spectra in the middle atmosphere. The main conclusions of this study are as follows.

1. Model-simulated spectra in the stratosphere and mesosphere have shape with a steep slope of $\sim m^{-3}$ at high values of m, consistent with observations reported in previous studies.

2. In a large part of the middle atmosphere, GWs are dominant in the m spectra only at high values of m, and disturbances other than GWs also contribute to the spectra at low values of m, even within the m^{-3} range.

3. The lowest value of m at which GWs are dominant is lower in the mesosphere than in the stratosphere.

4. Disagreement at low values of m between the spectra of GWs and those of all fluctuations is especially large in equatorial and polar regions.

Parameters describing the characteristics of GW spectra were also examined. The m_{g*} value of GW spectra is lower at higher altitudes. Parameter F_0, which reflects the spectral density at $m = m_{g*}$, is larger at higher altitudes. These vertical variations are consistent with wave saturation and the exponential decrease in density. Parameter t increases with height and approaches ~3 in mid- and high-latitude regions. In the lower stratosphere, the geographical distribution of F_0 is broadly consistent with the observations reported in previous studies. We also examined the shear effect on GW spectra below the eastward and westward jets. The results showed that strong vertical shear, in addition to wave saturation, contributes to making the slope of the GW spectra steeper.

The results reported in this study might have seasonal and interannual variations depending on varying background conditions such as the QBO in the equatorial region. To examine the universality of the results, it would be useful to perform similar simulations for other seasons and different years. The JAGUAR hindcasts contain three-dimensional and global data of GWs in the middle atmosphere. Such high–resolution and high–top model data represent a strong tool that could be used to quantitatively unveil GW behavior such as lateral propagation (e.g., Sato et al., 2009, 2012), intermittency (e.g., Hertzog et al., 2012; Alexander et al., 2016; Minamihara et al., 2020), secondary generation (e.g., Vadas & Becker, 2018; Yasui et al., 2018), and interaction with Rossby waves (e.g., Smith, 1996, 2003; Sato & Nomoto, 2015).

References

Alexander, M. J., & Dunkerton, T. J. (1999). A Spectral Parameterization of Mean-Flow Forcing due to Breaking Gravity Waves. *Journal of the Atmospheric Sciences*, **56**(24), 4167–4182. https://doi.org/10.1175/1520-0469(1999)056%3C4167:ASPOMF%3E2.0.CO;2

Alexander, S. P., Sato, K., Watanabe, S., Kawatani, Y., & Murphy, D. J. (2016). Southern Hemisphere extra-tropical gravity wave sources and intermittency revealed by a middle atmosphere General Circulation Model. *Journal of Atmospheric Sciences*, **73**, 1335–1349. https://doi.org/10.1175/JAS-D-15-0149.1

Allen, S. J., & Vincent, A. (1995). Gravity wave activity in the lower atmosphere: Seasonal and latitudinal variations. *Journal of Geophysical Research*, **100**, 1327– 1350. https://doi.org/10.1029/94JD02688

Bloom, S. C., Takacs, L. L., DaSilva, A. M., & Levina, D. (1996). Data assimilation using incremental analysis updates. *Monthly Weather Review*, **124,** 1256– 1271. https://doi.org/10.1175/1520-0493(1996)124<1256:DAUIAU>2.0.CO;2

Conn, A. R., Gould, N. I., & Toint, P. L. (2000). *Trust region methods*, Philadelphia, PA: Society for Industrial and Applied Mathematics. https://doi.org/10.1137/1.9780898719857

Dunkerton, T. J. (1981). On the inertial stability of the equatorial middle atmosphere. *Journal of Atmospheric Sciences*, **38**, 2354–2364. https://doi.org/10.1175/1520-0469(1981)038%3C2354:OTISFT%3E2.0.CO;2

Dewan, E. M., & Good, R. E. (1986). Saturation and the "universal" spectrum for vertical profiles of horizontal scalar winds in the atmosphere. *Journal of Geophysical Research*, **91**(D2), 2742–2748. https://doi.org/10.1029/JD091iD02p02742

Dewan, E. M., Grossbard, N., Quesada, A. F. & Good, R. E. (1984). Spectral analysis of 10m resolution scalar velocity profiles in the stratosphere. *Geophysical Research Letters*, **11**, 80–83. https://doi.org/10.1029/GL011i001p00080

Ern, M., Trinh, Q. T., Preusse, P., Gille, J. C., Mlynczak, M. G., Russell Iii, J. M., & Riese, M. (2018). GRACILE: a comprehensive climatology of atmospheric gravity wave parameters based on satellite limb soundings. *Earth System Science Data*, **10**, 857–892. https://doi.org/10.5194/essd-10-857-2018

Fritts, D. C., & Alexander, M. J. (2003). Gravity wave dynamics and effects in the middle atmosphere. *Reviews of Geophysics*, **41**, 1003. https://doi.org/10.1029/2001RG000106, 1.

Fritts, D. C., & Chou, H. (1987). An Investigation of the Vertical Wavenumber and Frequency Spectra of Gravity Wave Motions in the Lower Stratosphere. *Journal of Atmospheric Sciences*, **44**(24), 3610–3624. https://doi.org/10.1175/1520-0469(1987)044%3C3610:AIOTVW%3E2.0.CO;2

Hertzog, A., Alexander, M. J., & Plougonven, R. (2012). On the intermittency of gravity wave momentum flux in the stratosphere. *Journal of Atmospheric Sciences*, **69**(11), 3433–3448. https://doi.org/10.1175/JAS-D-12-09.1

Hines, C. O. (1997a). Doppler-spread parameterization of gravity-wave momentum deposition in the middle atmosphere. Part 1: Basic formulation. *Journal of Atmospheric and Solar-Terrestrial Physics*, **59**, 371–386. https://doi.org/10.1016/S1364-6826(96)00079-X

Hines, C. O. (1997b). Doppler-spread parameterization of gravity-wave momentum deposition in the middle atmosphere. Part 2: Broad and quasi monochromatic spectra, and implementation. *Journal of Atmospheric and Solar-Terrestrial Physics*, **59**(4), 387–400. https://doi.org/10.1016/S1364-6826(96)00080-6

Lindzen, R. S. (1981). Turbulence and stress owing to gravity wave and tidal breakdown. *Journal of Geophysical Research*, **86**, 9707–9714. https://doi.org/10.1029/JC086iC10p09707

Kawatani, Y., Sato, K., Dunkerton, T. J., Watanabe, S., Miyahara, S., & Takahashi, M. (2010a). The roles of equatorial trapped waves and internal inertia-gravity waves in driving the quasi-biennial oscillation. Part I: Zonal mean wave forcing. *Journal of Atmospheric Sciences*, **67**, 963–980. https://doi.org/10.1175/2009JAS3222.1

Kawatani, Y., Sato, K., Dunkerton, T. J., Watanabe, S., Miyahara, S., & Takahashi, M. (2010b). The roles of equatorial trapped waves and internal inertia-gravity waves in driving the quasi-biennial oscillation. Part II: Three-dimensional distribution of wave forcing. *Journal of Atmospheric Sciences*, **67**, 981–997. https://doi.org/10.1175/2009JAS3223.1

Koshin, D., Sato, K., Miyazaki, K., & Watanabe, S. (2020). An ensemble Kalman filter data assimilation system for the whole neutral atmosphere. *Geoscientific Model Development*, **13**, 3145–3177. https://doi.org/10.5194/gmd-13-3145-2020

Koshin, D., Sato, K., Kohma, M., & Watanabe, S. (2021). An update on the 4D-LETKF data assimilation system for the whole neutral atmosphere. *Geoscientific Model Development Discussion*. https://doi.org/10.5194/gmd-2020-381, in review.

Mayr, H. G., Mengel, J. G., Hines, C. O., Chan, K. L., Arnold, N. F., Reddy, C. A., & Porter, H. S. (1997). The gravity wave Doppler spread theory applied in a numerical spectral model of the middle atmosphere 2. Equatorial oscillations. *Journal of Geophysical Research*, **102**, 26,093–26,105. https://doi.org/10.1029/96JD03214

McLandress, C., & Scinocca, J. F. (2005). The GCM Response to Current Parameterizations of Nonorographic Gravity Wave Drag. *Journal of the Atmospheric Sciences*, **62**(7), 2394–2413. https://doi.org/10.1175/JAS3483.1

Minamihara, Y., Sato, K., & Tsutsumi, M. (2020). Intermittency of gravity waves in the Antarctic troposphere and lower stratosphere revealed by the PANSY radar observation. *Journal of Geophysical Research: Atmosphere*, **125**, e2020JD032543. https://doi.org/10.1029/2020JD032543.

Okamoto, K., Sato, K., & Akiyoshi, H. (2011). A study on the formation and trend of the Brewer-Dobson circulation. *Journal of Geophysical Research*, **116**, D10117. https://doi.org/10.1029/2010JD014953

Okui, H., Sato, K., Koshin, D., & Watanabe, S. (2021). Formation of a mesospheric inversion layer and the subsequent elevated stratopause associated with the major stratospheric sudden warming in 2018/19. *Journal of Geophysical Research: Atmospheres*, **126**, e2021JD034681. https://doi.org/10.1029/2021JD034681

Sato, K., & Dunkerton, T. J. (1997). Estimates of momentum flux associated with equatorial Kelvin and gravity waves. *Journal of Geophysical Research*, **102**, 26,247–26,261. https://doi.org/10.1029/96JD02514

Sato, K. & Hirano, S. (2019). The climatology of the Brewer–Dobson circulation and the contribution of gravity waves. *Atmospheric Chemistry and Physics*, **19**, 4517–4539. https://doi.org/10.5194/acp-19-4517-2019

Sato, K., & Nomoto, M. (2015). Gravity wave-induced anomalous potential vorticity gradient generating planetary waves in the winter mesosphere. *Journal of Atmospheric Sciences*, **72**, 3609–3624. https://doi.org/10.1175/JAS-D-15-0046.1.

Sato, K., Tateno, S., Watanabe, S., & Kawatani, Y. (2012). Gravity Wave Characteristics in the Southern Hemisphere Revealed by a High-Resolution Middle-Atmosphere General Circulation Model. *Journal of Atmospheric Sciences*, **69**, 1378–1396. https://doi.org/10.1175/JAS-D-11-0101.1.

Sato, K., Watanabe, S., Kawatani, Y., Tomikawa, Y., Miyazaki, K., & Takahashi, M. (2009). On the origins of mesospheric gravity waves. *Geophysical Research Letters*, **36**, L19801. https://doi.org/10.1029/2009GL039908

Sato, K., & Yamada, M. (1994). Vertical structure of atmospheric gravity waves revealed by the wavelet analysis. *Journal of Geophysical Research*, **99**(D10), 20,623–20,631. https://doi.org/10.1029/94JD01818

Sato, K., Yamamori, M., Ogino, S., Takahashi, N., Tomikawa, Y., & Yamanouchi, T. (2003). A meridional scan of the stratospheric gravity wave field over the ocean in 2001 (MeSSO2001). *Journal of Geophysical Research*, **108**(D16), 4491. https://doi.org/10.1029/2002JD003219

Smith, A. K. (1996). Longitudinal Variations in Mesospheric Winds: Evidence for Gravity Wave Filtering by Planetary Waves. *Journal of Atmospheric Sciences*, **53**, 1156–1173. https://doi.org/10.1175/1520-0469(1996)053<1156:LVIMWE>2.0.CO;2

Smith, A. K. (2003). The Origin of Stationary Planetary Waves in the Upper Mesosphere. *Journal of Atmospheric Sciences*, **60**, 3033–3041. https://doi.org/10.1175/1520-0469(2003)060<3033:TOOSPW>2.0.CO;2

Smith, S. A., Fritts, D. C., & Vanzandt, T. E. (1987). Evidence for a Saturated Spectrum of Atmospheric Gravity Waves. *Journal of Atmospheric Sciences*, **44**(10), 1404–1410. https://doi.org/10.1175/1520-0469(1987)044%3C1404:EFASSO%3E2.0.CO;2

Tsuda, T., Inoue, T., Kato, S., Fukao, S., Fritts, D. C., & VanZandt, T. E. (1989). MST Radar Observations of a Saturated Gravity Wave Spectrum. *Journal of Atmospheric Sciences*, **46**(15), 2440–2447. https://doi.org/10.1175/1520-0469(1989)046%3C2440:MROOAS%3E2.0.CO;2

Tsuda, T., Kato, S., Yokoi, T., Inoue, T., Yamamoto, M., Vanzandt, T. E., Fukao, S., & Sato, T. (1990). Gravity waves in the mesosphere observed with the middle and upper atmosphere radar. *Radio Science*, **25**(5), 1005–1018. https://doi.org/10.1029/RS025i005p01005

Vadas, S. L., & Becker, E. (2018). Numerical modeling of the excitation, propagation, and dissipation of primary and secondary gravity waves during wintertime at McMurdo Station in the Antarctic. *Journal of Geophysical Research: Atmosphere*, **123**, 9326–9369. https://doi.org/10.1029/2017JD027974

VanZandt, T. E. (1982). A universal spectrum of buoyancy waves in the atmosphere. *Geophysical Research Letters*, **9**, 575–578. https://doi.org/10.1029/GL009i005p00575

VanZandt, T. E. (1985). A model for gravity wave spectra observed by Doppler sounding systems. *Radio Science*, **20**(6), 1323–1330. https://doi.org/10.1029/RS020i006p01323

Warner, C. D., & McIntyre, M. E. (1996). On the Propagation and Dissipation of Gravity Wave Spectra through a Realistic Middle Atmosphere. *Journal of Atmospheric Sciences*, **53**(22), 3213–3235. https://doi.org/10.1175/1520-0469(1996)053%3C3213:OTPADO%3E2.0.CO;2

Warner, C. D. & McIntyre, M. E. (1999). Toward an ultra-simple spectral gravity wave parameterization for general circulation models. *Earth, Planets and Space*, **51**, 475–484. https://doi.org/10.1186/BF03353209

Watanabe, S. (2008). Constraints on a Non-orographic Gravity Wave Drag Parameterization Using a Gravity Wave Resolving General Circulation Model. *SOLA*, **4**, 61–64. https://doi.org/10.2151/sola.2008-016

Watanabe, S., & Miyahara, S. (2009). Quantification of the gravity wave forcing of the migrating diurnal tide in a gravity wave-resolving general circulation model. *Journal of Geophysical Research: Atmospheres*, **114**, D07110. https://doi.org/10.1029/2008JD011218

Yasui, R., Sato, K., & Miyoshi, Y. (2018). The momentum budget in the stratosphere, mesosphere, and lower thermosphere. Part II: The in situ generation of gravity waves. *Journal of Atmospheric Sciences*, **75**, 3635–3651. https://doi.org/10.1175/JAS-D-17-0337.1